nature climate change

Article

https://doi.org/10.1038/s41558-022-01555-7

# Reduced $CO_2$ uptake and growing nutrient sequestration from slowing overturning circulation

Received: 18 April 2022

Accepted: 15 November 2022

Published online: 22 December 2022

Check for updates

Y. Liu [1], J. K. Moore [1], F. Primeau [1] & W. L. Wang [2]

Current Earth system models (ESMs) project dramatic slowing (28–42% by 2100) of Atlantic Meridional Overturning Circulation and Southern Meridional Overturning Circulation (SMOC) across a range of climate scenarios, with a complete shutdown of SMOC possible by year 2300. Slowing meridional overturning circulation (MOC) differentially impacts the ocean biological and solubility carbon pumps, leaving the net impact on ocean carbon uptake uncertain. Here using a suite of ESMs, we show that slowing MOC reduces anthropogenic carbon uptake by the solubility pump but increases deep-ocean storage of carbon and nutrients by the biological pump. The net effect reduces ocean uptake of anthropogenic $CO_2$. The deep-ocean nutrient sequestration will increasingly depress global-scale, marine net primary production over time. MOC slowdown represents a positive feedback that could extend or intensify peak-warmth climate conditions on multi-century timescales.

The global meridional overturning circulation (MOC), comprised of the Atlantic-based upper MOC cell (AMOC) and the deeper Southern MOC cell (SMOC), strongly impacts climate and marine biogeochemistry[1–6]. Earth system models (ESM) from the Coupled Model Intercomparison Project phase 6 (CMIP6) project rapidly declining AMOC rates over the twenty-first century[6–8]. Recent observations suggest declining North Atlantic Deep Water (NADW) formation and slowing of AMOC are underway and already impacting biological productivity[9–11]. A recent study of 11 CMIP6 models found a strong link between Atlantic basin carbon storage and slowing AMOC[6]. There have been fewer studies of SMOC response to climate warming, particularly with ESM projections that extend beyond year 2100[12–15].

The oceans play a critical role in removing anthropogenic $CO_2$ from the atmosphere[16,17]. Global ocean dissolved inorganic carbon (DIC) concentrations have increased over time as the oceans take up anthropogenic $CO_2$, driven by rising atmospheric $CO_2$ concentrations[16,17]. Both the biological and solubility carbon pumps contribute to ocean $CO_2$ sequestration. The solubility pump refers to the combined influences of ocean circulation and inorganic carbon chemistry that contribute to uptake and storage of carbon dioxide, helping maintain observed vertical gradients of DIC (higher concentrations at depth). The biological pump refers to the biogenic export of carbon to the interior ocean (as sinking particulate organic carbon (POC), sinking calcium carbonate ($CaCO_3$) and transported dissolved organic matter), which modifies surface carbon chemistry and air–sea $CO_2$ exchange. CMIP phase 5 ESMs project weakening biological carbon export from surface waters over the twenty-first century, generally with larger decreases under stronger warming scenarios[18–20].

Slowing MOC weakens carbon uptake by the solubility pump but allows more time for exported biogenic carbon to accumulate at depth, increasing deep-ocean carbon and nutrient storage by the biological pump[2–6,21–26]. Previous studies often focused on a single model, assumed steady-state circulation or focused on the palaeoclimate context. MOC impacts on global ocean carbon uptake and the underlying mechanisms across multiple warming scenarios remain unclear, as all these multiple processes are integrated in ESMs and the relative roles of these processes may be changing over time, making it difficult to disentangle. Here we diagnose the effects of slowing overturning circulation on the ocean carbon sink in the context of a warming climate with a suite of CMIP6 ESM projections along three potential future climate scenarios.

[1]Department of Earth System Science, University of California Irvine, Irvine, CA, USA. [2]State Key Laboratory of Marine Environmental Science, College of Ocean and Earth Sciences, Xiamen University, Xiamen, China. e-mail: yil45@uci.edu; jkmoore@uci.edu

 https://doi.org/10.1038/s41558-022-01555-7

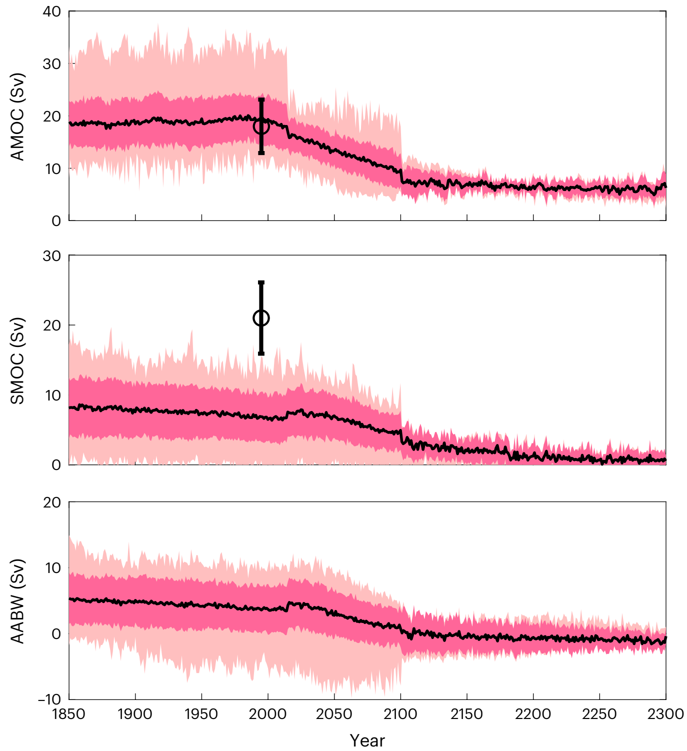


**Fig. 1 | Slowing MOC with strong climate warming.** Mean MOC rates (Sv) under the SSP5–8.5 scenario from CMIP6 models to year 2300 (36 models for historical period, 28 extend to 2100, 6 models extend to 2300; Supplementary Table 1) are shown for AMOC (top) and SMOC (middle). Black line indicates the CMIP6 multi-model mean, and light and dark pink shadings indicate the range and one standard deviation. Black circles and lines indicate mean and one standard deviation of the observation-based MOC estimates in Supplementary Table 3. Also shown is the mean northward bottom flow across 50° S (>4,000 m), representing export of Antarctic Bottom Water (AABW) from the Southern Ocean (Supplementary Information provides details).

We also incorporate a new offline model based on output from the community Earth System Model (CESM)v1(BGC) CMIP5 representative concentration pathways (RCP)8.5– extended concentration pathways (ECP)8.5 simulation[12] (hereafter CESMv1-RCP8.5). Simulations with the offline model allow us to more accurately diagnose the changing contributions of different processes to carbon sequestration over time in the CESMv1-RCP8.5 simulation (Methods).

## Climate warming slows MOC

We calculate the changing rates of overturning in AMOC and SMOC for a suite of 36 CMIP6 models and 24 CMIP5 models to year 2100 across multiple climate scenarios (CMIP5 RCP8.5 and CMIP6 SSPs 1–2.6, 2–4.5 and 5–8.5). Radiative forcing at 2100 is the same for the two high-end scenarios but with a modestly different relative contribution from different greenhouse gases. We extend this analysis to year 2300 for the six CMIP6 models with output available on the Earth System Grid Federation (ESGF) (Supplementary Tables 1 and 2). The RCP8.5 and SSP5–8.5 are high-end warming, emissions-as-usual scenarios; SSP2–4.5 has more moderate warming; and SSP1–2.6 is a stabilization scenario aimed at keeping mean surface warming below 2 °C (ref. 8). The CMIP6 mean AMOC rate (maximum overturning at 30° N) for the present climate (1990s) is 19.2 ± 4.5 Sv, which matches well with the estimate of 17.0 ± 4.4 Sv from the RAPID project[27] and other observation-based estimates[28] (Fig. 1 and Supplementary Table 3). However, all CMIP6 models underestimate SMOC rate (maximum overturning at 30° S) compared to the observational estimates (Fig. 1, Extended Data Fig. 1 and Supplementary Table 3). Despite these model discrepancies, there is a robust trend across the models of declining overturning rates in both AMOC and SMOC as the climate warms.

There is a dramatic future slowing of both MOC cells on the high-end warming scenarios (RCP8.5, SSP5–8.5) that extends well beyond year 2100 (Fig. 1 and Extended Data Fig. 1). The CMIP6 model mean AMOC rate steadily declines over the twenty-first century (ref. 6) before stabilizing at a much-reduced rate (Fig. 1a), similar to the CMIP5 models (Extended Data Fig. 1). Overturning rates for both MOC cells also decline to year 2100 under the more moderate warming scenarios (Fig. 2 and Extended Data Fig. 1). SMOC slows as polar salinity-driven stratification intensifies (Extended Data Fig. 2 and Supplementary Fig. 1) and appears to be shutting down completely by year 2300 in available CMIP6 SSP5–8.5 models, similar to the pattern in the CESMv1-RCP8.5 simulation (Fig. 1, Extended Data Fig. 1 and Supplementary Fig. 1). Both AMOC and SMOC slow with climate warming, but there is a range of responses across models and climate scenarios (Figs. 1 and 2 and Table 1). There is considerable variability in the degree of MOC slowdown, with the inter-model differences often larger than the variability across different climate scenarios with the same model. Thus, there is broad agreement in projecting rapidly declining MOC rates this century, but substantial uncertainty remains in the magnitude of MOC slowing and in the tipping points related to potential MOC shutdown in the centuries beyond.

## Reduced ocean carbon uptake from slowing SMOC

To understand the time-dependent contributions of the biological and solubility pumps to global ocean carbon uptake, we partition DIC into the regenerated and pre-formed components using the apparent oxygen utilization (AOU) and define the strength of the biological and solubility carbon pumps in a changing climate as the accumulation rate of the regenerated DIC and pre-formed DIC, respectively, relative to the pre-industrial for 13 CMIP6 models and the CESMv1-RCP8.5 simulation.

We find increasing ocean carbon storage (full depth) in every model with most of the accumulation as pre-formed DIC at intermediate depths (100–2,000 m; Fig. 2 and Table 1). The whole ocean regenerated DIC storage ranges widely across these models from +5 Pg C to +142 Pg C, accounting for 1% to 30% (mean 15%) of the total ocean carbon storage by 2100 (Fig. 2). Yet in the deep ocean (>2,000 m), regenerated DIC accounted for ~50–100% of the carbon accumulation and increases over the twenty-first century across the CMIP6 models and different warming scenarios (Fig. 2, Extended Data Figs. 3–5 and Table 1). Differences in deep-ocean regenerated carbon accumulation are limited across the warming scenarios, even though both AMOC and SMOC tend to slow more with stronger climate warming (Table 1). Storage of pre-formed carbon in the deep ocean increases at a slower rate or in some models declines over the twenty-first century (Fig. 2 and Extended Data Figs. 3–5). Thus, the biological pump is coming to dominate deep-ocean (>2,000 m) carbon storage by 2100 in most of the CMIP6 models, particularly under stronger climate warming scenarios (SSP2–4.5 and SSP5–8.5 scenarios).

Regenerated DIC is also accumulating at intermediate depths, but this accumulation scales more strongly with degree of climate warming across the CMIP6 scenarios (Fig. 2 and Table 1). The accumulation of regenerated DIC by the end of this century is correlated with the changes in export production normalized by the slowdown of SMOC because the accumulation of regenerated DIC is controlled by the changes in surface export production, which injects carbon into ocean interior, and by the changes of SMOC, which is an indicator of ocean interior residence time and the potential to accumulate regenerated DIC. This correlation is valid across CMIP6 SSP1–2.6, SSP2–4.5 and SSP5–8.5 warming scenarios (Fig. 3). Furthermore, it is also valid in the intermediate and deep ocean (Extended Data Figs. 6 and 7).

We hypothesize that slowing of the MOC will reduce the capacity of the oceans to take up anthropogenic $CO_2$ on multi-century timescales

 https://doi.org/10.1038/s41558-022-01555-7

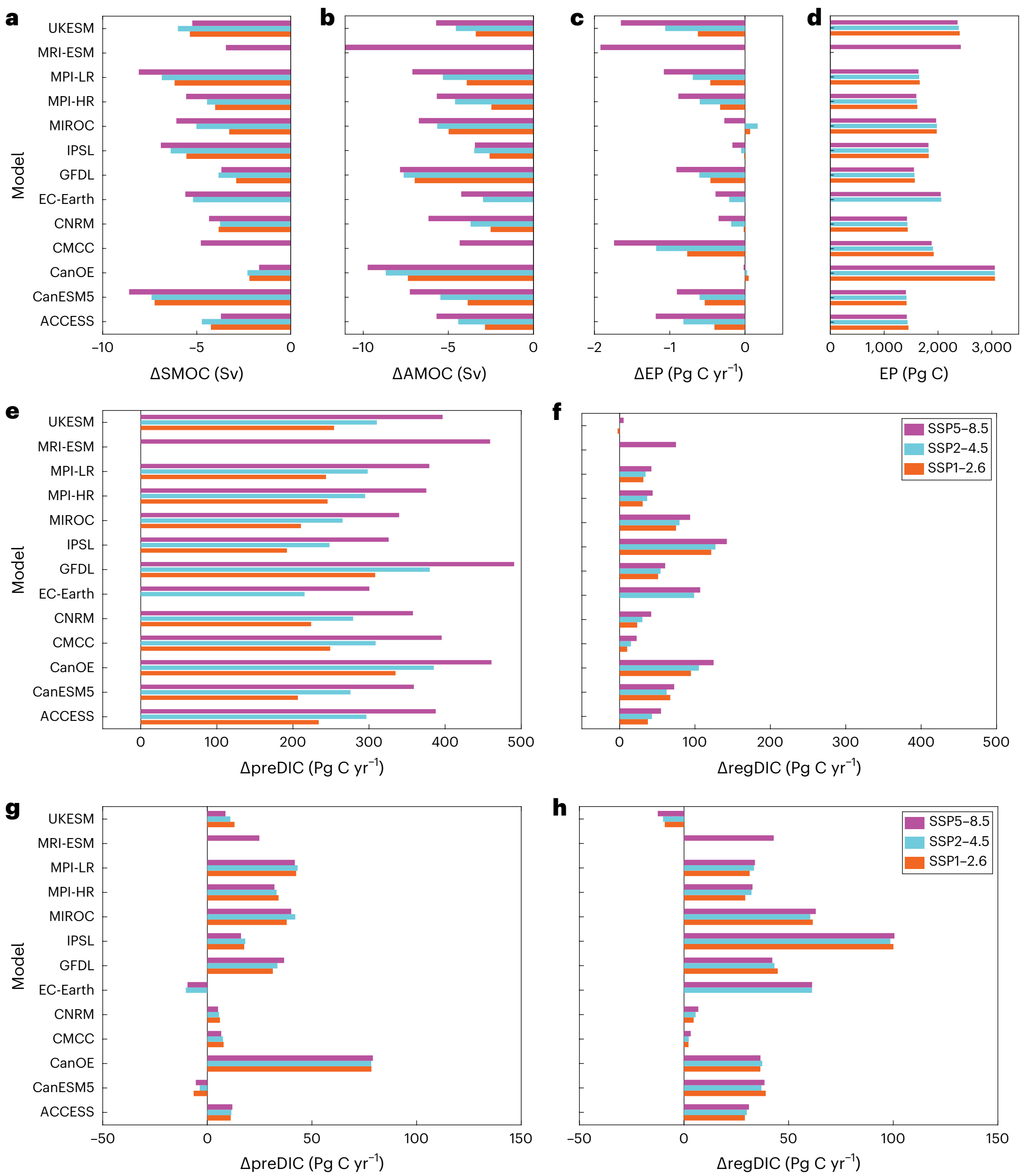


**Fig. 2 | Changes in meridional overturning, carbon export and carbon storage by 2100. a**,**b**, Changes in SMOC and AMOC (Sv) comparing pre-industrial mean 1850–1869 to mean of years 2090–2099. **c**, Changes in export production (EP; sinking organic carbon) at 100 m (Pg C yr$^{-1}$). **d**, Integrated export production from 1850 to 2100 (Pg C). **e**,**f**, Pre-formed (preDIC) and regenerated carbon (regDIC) accumulation (Pg C yr$^{-1}$) at intermediate depths (100–2,000 m) under three warming scenarios. **g**,**h**, Deep-ocean carbon accumulation (>2,000 m) as in **e** and **f**. For reference, 1 ppm atmospheric $CO_2$ = 0.47 Pg C. Only 13 models with necessary variables are included.

in the context of increasing atmospheric $CO_2$. Slowing SMOC should weaken the solubility pump, as it controls ventilation of the ocean interior on multi-century timescales. Great amounts of pre-formed DIC are accumulating at intermediate depths (100–2,000 m) in CMIP6, but little of this is making it into the deep ocean, in part due to slowing MOC (Fig. 2 and Table 1). We find strong correlations between the slowing of SMOC and both pre-formed and total ocean DIC storage by 2100 across CMIP6 SSP1–2.6, SSP2–4.5 and SSP5–8.5 projections for models with necessary output available on the ESGF (Fig. 3). The models with the greatest slowing of SMOC take up the least pre-formed and total DIC. The declines in SMOC can explain 39–51% of the variance in ocean carbon storage by the solubility pump by 2100, depending on the warming scenarios (Fig. 3). The storage of regenerated DIC only partially makes up the difference between pre-formed and total DIC storage (Fig. 3). If we consider intermediate and deep ocean separately, the same correlation holds true in the intermediate ocean (Extended Data Fig. 6), but in the deep ocean, the correlation becomes much weaker as the deep ocean has longer ventilation time which does not allow as much pre-formed DIC accumulation in the deep ocean by 2100, and the impacts of slowing SMOC on regenerated DIC and pre-formed DIC partially cancel out, resulting in no obvious correlation to total DIC (Extended Data Fig. 7).

We examine centennial-timescale changes in carbon and nutrient accumulation rates (relative to pre-industrial) in the CESMv1-RCP8.5 to better illustrate processes happening across the CMIP6 models. DIC storage rate peaks in the twenty-first century and declines in ocean

https://doi.org/10.1038/s41558-022-01555-7

**Table 1 | CMIP6 model mean changes in physical and biogeochemical fluxes by 2100 under three climate scenarios**

| | SSP1–2.6 | SSP2–4.5 | SSP5–8.5 |
|---|---|---|---|
| ΔAMOC (Sv) | −5.1±3.0 | −6.0±2.6 | −7.3±2.7 |
| | (−28.8±16.4%) | (−33.6±14.2%) | (−41.7±13.8%) |
| | ($n$=24) | ($n$=26) | ($n$=28) |
| ΔSMOC (Sv) | −3.6±1.9 | −4.0±2.0 | −4.6±2.3 |
| | (−33.2±14.1%) | (−37.9±13.7%) | (−41.9±14.8%) |
| | ($n$=24) | ($n$=26) | ($n$=28) |
| ΔEP (Pg C yr$^{-1}$) | −0.4±0.2 | −0.6±0.3 | −1.1±0.5 |
| | (−4.5±4.0%) | (−6.9±5.7%) | (−12.3±8.2%) |
| | ($n$=11) | ($n$=12) | ($n$=13) |
| ΔpreDIC (100–2,000 m, Pg C yr$^{-1}$) | 220.5±32.1 | 273.6±37.1 | 364.2±46.6 |
| | ($n$=11) | ($n$=12) | ($n$=13) |
| ΔpreDIC (>2,000 m, Pg C yr$^{-1}$) | 24.4±24.0 | 22.1±25.1 | 21.8±24.4 |
| | ($n$=11) | ($n$=12) | ($n$=13) |
| ΔregDIC (100–2,000 m, Pg C yr$^{-1}$) | 15.9±16.7 | 21.7±18.1 | 31.7±20.1 |
| | ($n$=11) | ($n$=12) | ($n$=13) |
| ΔregDIC (>2,000 m, Pg C yr$^{-1}$) | 34.0±30.1 | 36.3±29.3 | 37.3±28.7 |
| | ($n$=11) | ($n$=12) | ($n$=13) |

Shown are the mean changes in MOC rates and in the sinking flux of particulate organic carbon at 100 m depth from CMIP6 models (2080–2099 mean relative to 1850–1869 mean for each model) across a range of warming scenarios. For each calculation, we include all CMIP6 models with all necessary output available on the ESGF. $n$ is the number of models with necessary variables.

uptake out to year 2300 (Fig. 4). The accumulation of DIC is initially much larger in surface waters than at depth, due to direct uptake of anthropogenic $CO_2$ from the atmosphere. However, the movement of carbon from the surface to the interior by circulation eventually dominates over the transfer of carbon from the atmosphere to the oceans, causing the relative contribution of surface ocean DIC storage to decrease. The strongest accumulation rate progressively shifts to intermediate-depth waters (Fig. 4). Pre-formed DIC dominates accumulation at intermediate depths (100–2,000 m), but little has reached the deep ocean, even by 2300, largely due to slowing MOC (Fig. 4 and Table 1). Pre-formed DIC accumulation rates decline at all depth levels after 2100, with very little accumulation in the deep ocean and no surface accumulation (<100 m) of pre-formed DIC in the 2200s. The accumulation rate of pre-formed DIC at intermediate depths slows substantially in the 2200s compared with the previous two centuries but still accounts for most of the total carbon storage over the twenty-third century (Fig. 4).

During the twentieth century, CESMv1-RCP8.5 accumulation of carbon in the deep ocean (>2,000 m) is dominated by the solubility pump (~67%), but the biological pump comes to dominate deep-ocean carbon storage (Fig. 4). By 2100, the biological pump accounts for 65% of the deep-ocean DIC accumulation, increasing to 85% by 2300 (Fig. 4). Thus, the biological pump comes to dominate deep-ocean carbon storage with strong climate warming in the CESMv1-RCP8.5, as seen in the CMIP6 models (Fig. 2 and Extended Data Figs. 3–5). The biological pump is also sequestering nitrate and phosphate in the deep ocean, with large upper-ocean declines balanced by increasing deep-ocean concentrations (Fig. 4). In 2200s, both the pre-formed and regenerated DIC keep accumulating in the ocean, but the declines of accumulation rates of pre-formed DIC are far larger than the declines in regenerated DIC accumulation rates compared with the 2100s (Fig. 4). Thus, the total rate of $CO_2$ uptake from the atmosphere is declining just as atmospheric $CO_2$ concentrations and surface temperatures are approaching peak values[8,12].

To better understand the changing regenerated DIC distributions, we separate the effects of decreasing surface export flux from the effects of slowing MOC on regenerated carbon distributions with the offline model. We perform a decomposition of the carbon accumulation using offline simulations in which the biological source terms and the circulation are prescribed factorially to be either time varying or fixed to their pre-industrial values (1850s) as simulated with the online ESM (Supplementary Information). These offline simulations provide a clean separation of the influences of time-varying physical and biological processes. We diagnose the carbon fluxes for CESMv1-RCP8.5 with the offline model, separating the contributions of sinking biological fluxes and the time-varying ocean circulation fluxes across the 100 m and 2,000 m depth horizons, comparing the steady-state pre-industrial fluxes with the changing accumulation rates averaged over the twenty-first and twenty-third centuries (Fig. 5). The sinking biogenic carbon fluxes at both depths decline over time by ~30%. However, the return of deep ocean, regenerated DIC back to the surface by the circulation declines even more, from 0.76 Pg C yr$^{-1}$ pre-industrial to 0.38 Pg C yr$^{-1}$ in the twenty-first century and even brings (−0.04 Pg C yr$^{-1}$) upper-ocean regenerated DIC back to the deep ocean in the twenty-third century (Fig. 5). The imbalance leads to net storage of regenerated carbon, nitrogen and phosphorus in the deep ocean, depressing upper-ocean nutrient concentrations (Figs. 4 and 5). With available model output, we could separate the impacts of changing surface export and circulation on regenerated DIC accumulation for CESMv1-RCP8.5 and for three CMIP6 projections. In each of these projections the biological export from surface waters declines over the twenty-first century. Thus, all of the increasing deep-ocean regenerated DIC accumulation is due to slowing MOC (Extended Data Fig. 8 and Table 1).

## Discussion and conclusions

The CMIP6 ESMs consistently project dramatic slowing of AMOC and SMOC across a wide range of future climate scenarios. There are substantial differences across the models in both the magnitude of MOC slowing and in how strongly it scales with the degree of climate warming (Figs. 1 and 2 and Extended Data Figs. 1 and 2). On the low-end warming scenario (SSP1–2.6), both MOC cells stabilize after year 2100 but at rates greatly reduced from the pre-industrial (−37% for AMOC, −67% for SMOC). There are no signs of MOC recovery by year 2300. On the high-end warming scenario (SSP5–8.5), SMOC appears to collapse completely by 2300 (Fig. 1 and Supplementary Fig. 1).

Slowing MOC increases the efficiency of the biological pump. Global-scale primary production and surface biogenic carbon export will decline as critical nutrients are increasingly sequestered in the deep ocean, along with community shifts from larger phytoplankton to smaller phytoplankton under increasing nutrient stress[12,19] until at some point MOC becomes more vigorous again[13]. Despite the declining or flat surface export production, nearly all of the models show increasing storage of regenerated DIC over this century, due to the MOC slowing (Fig. 2, Extended Data Fig. 8 and Table 1). In the near term, the increasing sequestration efficiency of the biological pump, driven by the MOC slowdown, leads to net removal of $CO_2$ from the atmosphere, partially compensating for the weakening solubility pump. However, a substantial pulse of $CO_2$ could be released back to the atmosphere when a more vigorous MOC eventually returns. Some studies have suggested a returning MOC strength after several hundred years[13,21,22,29–31]. These coarse-resolution and intermediate-complexity models did not include active ice sheets and may not accurately capture the long-term climate

https://doi.org/10.1038/s41558-022-01555-7

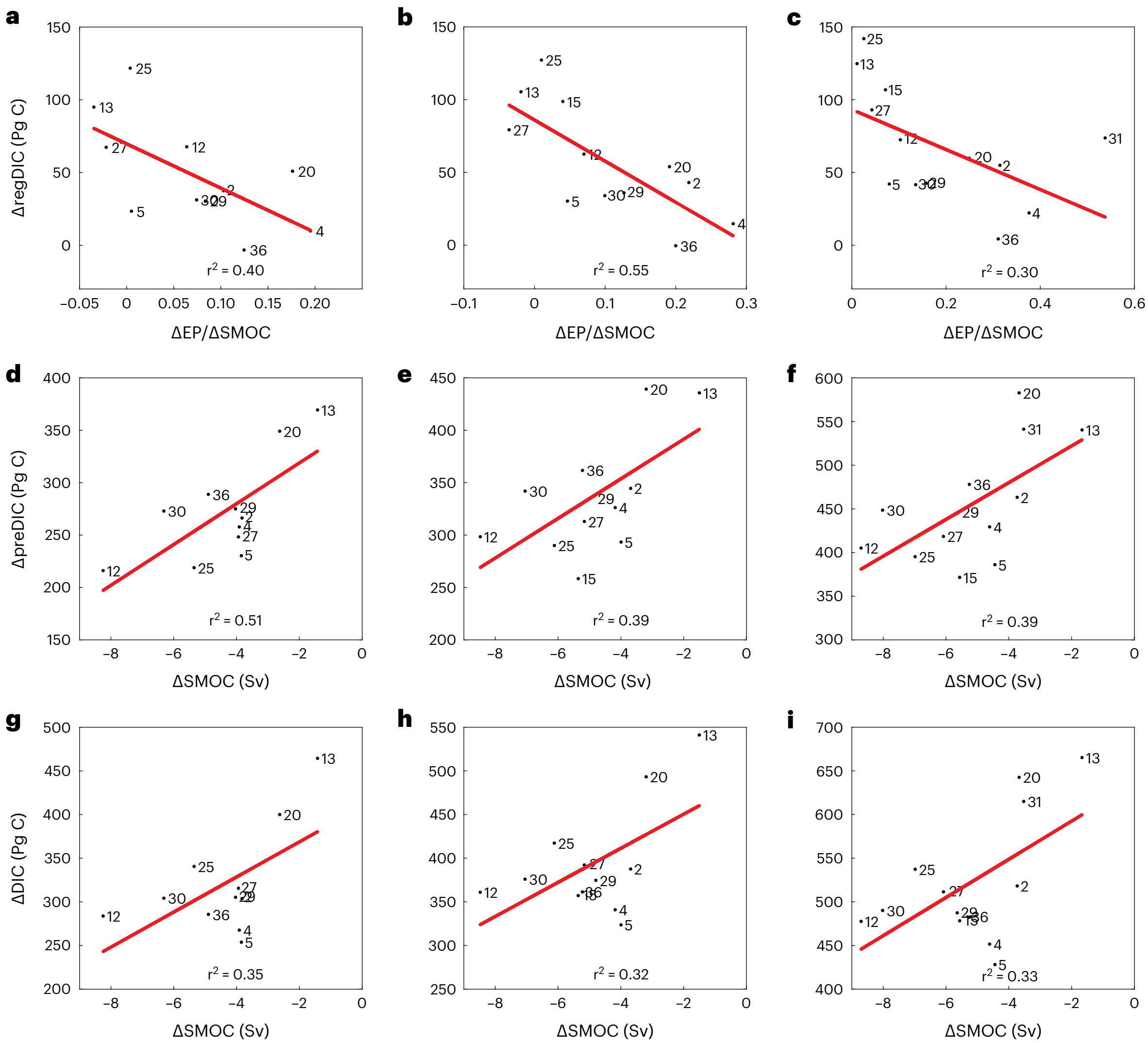


**Fig. 3 | Slowing SMOC rates reduce ocean carbon uptake. a–i**, The full water column storage of regenerated dissolved inorganic carbon (**a**–**c**), pre-formed DIC (**d**–**f**) and total DIC (**g**–**i**) by year 2100 (2080–2099 compared with 1850–1869) from 11 CMIP6 SSP1–2.6 projections (**a**,**d**,**g**), 12 CMIP6 SSP2–4.5 projections (**b**,**e**,**h**) and 13 CMIP6 SSP5–8.5 projections (**c**,**f**,**i**) are compared with the relative declines of export production and SMOC rates (regenerated DIC) and declines in SMOC rate (pre-formed DIC and total DIC) by year 2100 (2080–2099 compared with 1850–1869). Plotted numbers indicate the model number in Supplementary Table 1. Red lines show regression lines and $r^2$.

impacts on MOC. The longer residence time in the deep ocean allows more accumulation of regenerated carbon and nutrients at depth, but it also allows more oxygen to be consumed before water masses are again ventilated at the surface. Slowing MOC will exacerbate the expected declines in ocean oxygen content, driven primarily by warming effects on solubility and increasing upper-ocean stratification[26,32]. MOC shutdown could eventually lead to an anoxic deep ocean, which has contributed to past mass extinction events[33].

Slowing MOC weakens the solubility pump's capacity to take up and store anthropogenic $CO_2$ on multi-century timescales. The increasing efficiency of the biological pump only partially compensates for much larger decreases in solubility pump efficiency (that is, pre-formed DIC accumulation) as circulation changes and surface waters saturate with $CO_2$ (Figs. 2–5). Thus, slowing of MOC with climate warming will weaken ocean uptake of $CO_2$, potentially extending hot climate conditions by hundreds to even thousands of years[34–39]. Elevated air temperatures and high $CO_2$ concentrations could last for millennia with a persistent collapse of MOC, which would prevent the deep ocean from contributing to $CO_2$ drawdown. The timescale for AABW to return to the surface had already increased by 2000 years as of the 2090s due to the rapid slowing of SMOC in one ESM[35]. The intermediate-complexity models used to generate the CMIP6 climate scenarios lack realistic ocean circulation[8] and so likely overestimate ocean $CO_2$ uptake by not properly accounting for the impacts of MOC slowdown as climate warms. This means larger reductions in greenhouse gas emissions than previously estimated may be necessary to achieve the targeted radiative forcing trends, and for the more moderate scenarios, the climate stabilization goals.

Millennial-timescale ESM projections are necessary to understand the impacts of global warming on ocean circulation, biogeochemistry and marine ecosystems and to evaluate associated potential climate feedbacks and tipping points[34–40]. However, few previous studies have included active ice-sheet dynamics and so are missing the massive freshwater inputs from Greenland and Antarctica that will come with climate warming and the corresponding impacts on ocean circulation and biogeochemistry[41–44]. These freshwater inputs will further stratify polar regions, inhibiting deep water formation. Thus, inclusion of active ice-sheet dynamics in the ESMs will probably further weaken MOC[32] relative to the CMIP6 results presented here, potentially contributing to a shutdown of the deep water formation that drives both

https://doi.org/10.1038/s41558-022-01555-7

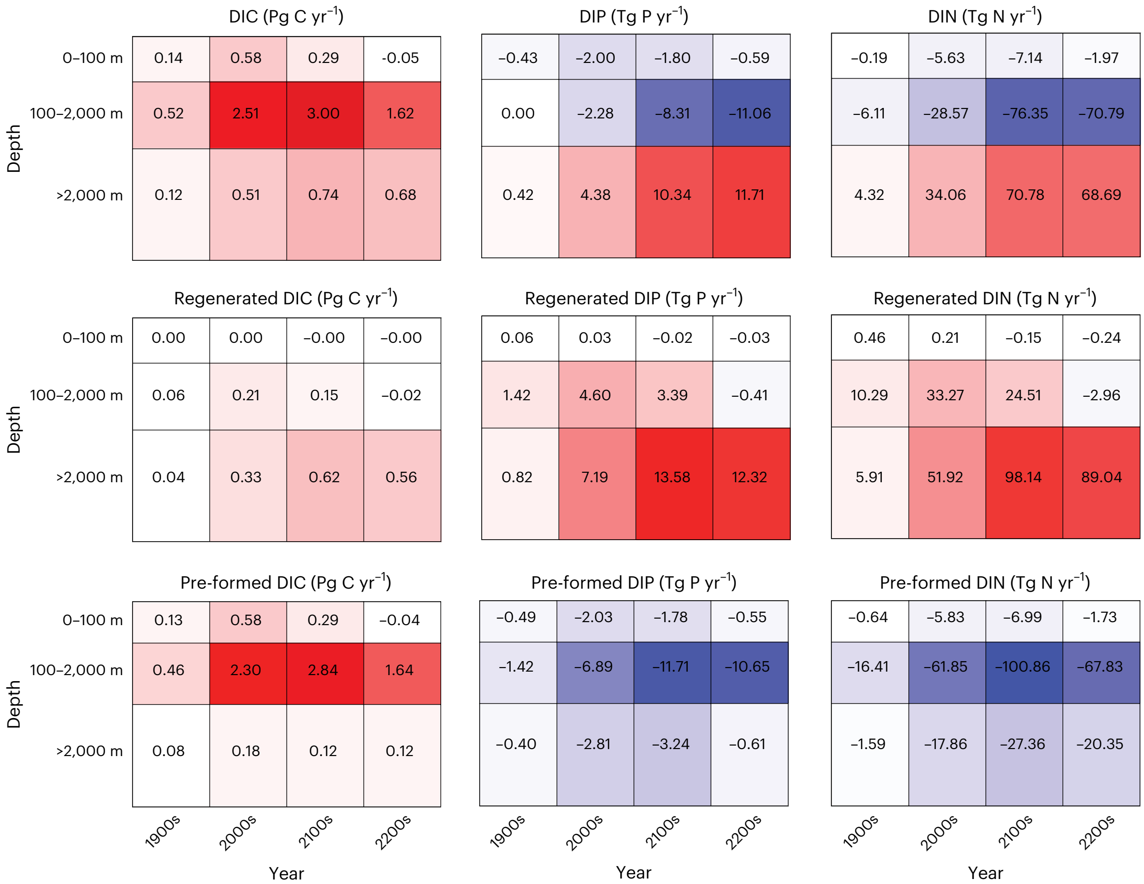


**Fig. 4 | Shifting carbon and nutrient distributions over time with climate warming.** CESMv1-RCP8.5 centennial mean accumulation rates of dissolved inorganic carbon (left column, DIC (Pg C yr$^{-1}$)), dissolved inorganic phosphorus (middle column, DIP (Tg P yr$^{-1}$)) and dissolved inorganic nitrogen (right column, DIN (Tg N yr$^{-1}$)) in the surface ocean (0–100 m), intermediate depths (100–2,000 m) and deep ocean (>2,000 m) averaged over the periods 1901–2000, 2001–2100, 2101–2200 and 2201–2300 under the RCP8.5–ECP8.5 scenario. The regenerated and pre-formed components sum to totals shown in top row. Red and blue shadings indicate positive and negative accumulation rates, respectively.

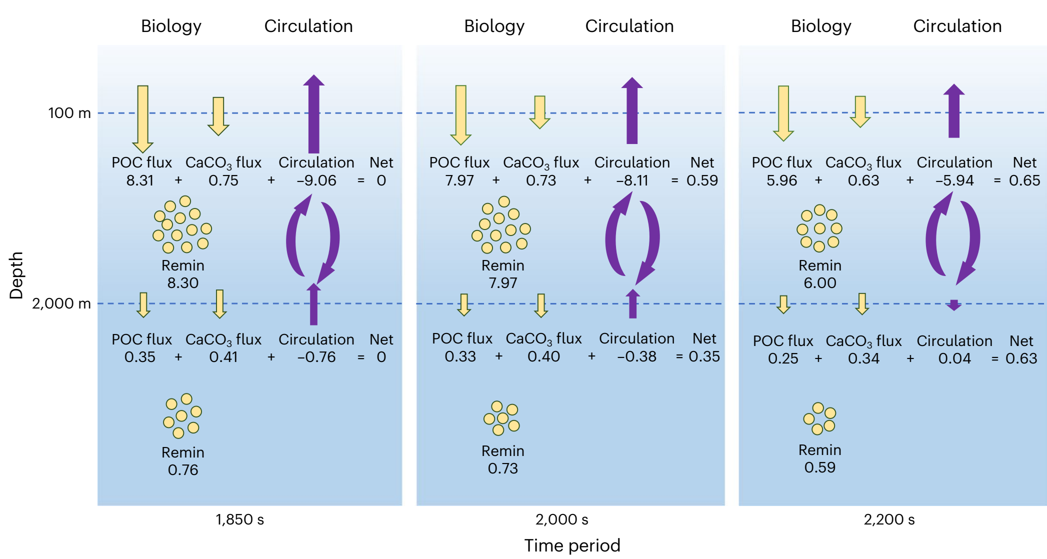


**Fig. 5 | Biological export and changing circulation contributions to regenerated carbon storage.** CESMv1-RCP8.5 carbon fluxes across the 100 m and 2,000 m depth horizons due to biology as sinking POC and calcium carbonate ($CaCO_3$) (yellow arrows) and physical transport across these depths due to circulation and mixing (purple arrows) under the RCP8.5–ECP8.5 scenario (Pg C yr$^{-1}$). Remin means remineralization. Left, middle and right panels show mean carbon fluxes for the pre-industrial (1850s) and the periods 2001–2100 and 2201–2300, respectively.

MOC cells. Some CMIP6 models form AABW through an unrealistic, open-ocean convection, missing important shelf and coastal processes that influence AABW in the observations, including dynamic ocean–ice-sheet interactions[15]. Deep water formation results from complex interactions between the oceans, the atmosphere, sea ice and ice sheets, often at spatial scales smaller than current ESM grid cells can represent. Improved representation of the deep water formation processes that drive the MOC cells should be a top priority for ESM development[6,14,15] as these processes will largely determine the long-term trajectory of ongoing climate perturbation. As humanity moves to reduce greenhouse emissions, there is a great need to explore millennial-timescale climate change with state-of-the-art ESMs to better understand the full consequences of greenhouse gas emissions for planet Earth[12,13,34–39].

## Online content

Any methods, additional references, Nature Portfolio reporting summaries, source data, extended data, supplementary information, acknowledgements, peer review information; details of author contributions and competing interests; and statements of data and code availability are available at https://doi.org/10.1038/s41558-022-01555-7.

## References

1. Jahn, A. & Holland, M. M. Implications of Arctic sea ice changes for North Atlantic deep convection and the meridional overturning circulation in CCSM4-CMIP5 simulations. *Geophys. Res. Lett.* **40**, 1206–1211 (2013).
2. Matear, R. J. & Hirst, A. C. Climate change feedback on the future oceanic $CO_2$ uptake. *Tellus B Chem. Phys. Meteorol.* **51**, 722–733 (1999).
3. Plattner, G. K., Joos, F., Stocker, T. F. & Marchal, O. Feedback mechanisms and sensitivities of ocean carbon uptake under global warming. *Tellus B Chem. Phys. Meteorol.* **53**, 564–592 (2001).
4. Schmittner, A. Decline of the marine ecosystem caused by a reduction in the Atlantic overturning circulation. *Nature* **434**, 628–633 (2005).
5. Whitt, D. B. & Jansen, M. F. Slower nutrient stream suppresses Subarctic Atlantic Ocean biological productivity in global warming. *Proc. Natl Acad. Sci. USA* **117**, 15504–15510 (2020).
6. Katavouta, A. & Williams, R. G. Ocean carbon cycle feedbacks in CMIP6 models: contributions from different basins. *Biogeosciences* **18**, 3189–3218 (2021).
7. Weijer, W., Cheng, W., Garuba, O. A., Hu, A. & Nadiga, B. T. CMIP6 models predict significant 21st century decline of the atlantic meridional overturning circulation. *Geophys. Res. Lett.* **47**, e2019GL086075 (2020).
8. O'Neill, B. C. O. et al. The scenario model intercomparison (ScenarioMIP) for CMIP6. *Geosci. Model Dev.* **9**, 3451–3482 (2016).
9. Thornalley, D. J. R. et al. Anomalously weak Labrador Sea convection and Atlantic overturning during the past 150 years. *Nature* **556**, 227–230 (2018).
10. Caesar, L., Rahmstorf, S., Robinson, A., Feulner, G. & Saba, V. Observed fingerprint of a weakening Atlantic Ocean overturning circulation. *Nature* **556**, 191–196 (2018).
11. Osman, M. B. et al. Industrial-era decline in subarctic Atlantic productivity. *Nature* **569**, 551–555 (2019).
12. Moore, J. K. et al. Sustained climate warming drives declining marine biological productivity. *Science* **359**, 1139–1143 (2018).
13. Frölicher, T. L. et al. Contrasting upper and deep ocean oxygen response to protracted global warming. *Glob. Biogeochem. Cycles* **34**, e2020GB006601 (2020).
14. Beadling, L. R. et al. Representation of Southern Ocean properties across Coupled Model Intercomparison Project generations: CMIP3 to CMIP6. *J. Clim.* **33**, 6555–6581 (2020).
15. Heuzé, C. Antarctic bottom water and North Atlantic deep water in CMIP6 models. *Ocean Sci.* **17**, 59–90 (2021).
16. Sabine, C. L. et al. The oceanic sink for anthropogenic $CO_2$. *Science* **305**, 367–371 (2004).
17. Gruber, N. et al. The oceanic sink for anthropogenic $CO_2$ from 1994 to 2007. *Science* **363**, 1193–1199 (2019).
18. Bopp, L. et al. Multiple stressors of ocean ecosystems in the 21st century: projections with CMIP5 models. *Biogeosciences* **10**, 6225–6245 (2013).
19. Fu, W., Randerson, J. T. & Moore, J. K. Climate change impacts on net primary production (NPP) and export production (EP) regulated by increasing stratification and phytoplankton community structure in the CMIP5 models. *Biogeosciences* **13**, 5151–5170 (2016).
20. Laufkötter, C. et al. Projected decreases in future marine export production: the role of the carbon flux through the upper ocean ecosystem. *Biogeosciences* **13**, 4023–4047 (2016).
21. Frölicher, T. & Joos, F. Reversible and irreversible impacts of greenhouse gas emissions in multi-century projections with the NCAR global coupled carbon cycle–climate model. *Clim. Dyn.* **35**, 1439–1459 (2010).
22. Bernardello, R., Marinov, I., Palter, J. B., Galbraith, E. D. & Sarmiento, J. L. Impact of Weddell Sea deep convection on natural and anthropogenic carbon in a climate model. *Geophys. Res. Lett.* **41**, 7262–7269 (2014).
23. Ito, T. Sustained growth of the Southern Ocean carbon storage in a warming climate. *Geophys. Res. Lett.* **42**, 4516–4522 (2015).
24. DeVries, T., Holzer, M. & Primeau, F. Recent increase in oceanic carbon uptake driven by weaker upper-ocean overturning. *Nature* **542**, 215–218 (2017).
25. Ödalen, M., Nycander, J., Oliver, K. I. C., Brodeau, L. & Ridgwell, A. The influence of the ocean circulation state on ocean carbon storage and $CO_2$ drawdown potential in an Earth system model. *Biogeosciences* **15**, 1367–1393 (2018).
26. Koeve, W., Kähler, P. & Oschllies, A. Does export production measure transient changes of the biological carbon pump's feedback to the atmosphere under global warming? *Geophys. Res. Lett.* **47**, e2020GL089928 (2020).
27. Frajka-Williams, E. et al. Atlantic Meridional Overturning Circulation: observed transport and variability. *Front. Mar. Sci.* **6**, 260 (2019).
28. Cessi, P. The global overturning circulation. *Annu. Rev. Mar. Sci.* **11**, 249–270 (2019).
29. Schmittner, A., Oschlies, A., Matthews, H. D. & Galbraith, E. D. Future changes in climate, ocean circulation, ecosystems, and biogeochemical cycling simulated for a business-as-usual $CO_2$ emission scenario until year 4000 AD. *Glob. Biogeochem. Cycles* **22**, GB1013 (2008).
30. Yamamoto, A. et al. Global deep ocean oxygenation by enhanced ventilation in the Southern Ocean under long-term global warming. *Glob. Biogeochem. Cycles* **29**, 1801–1815 (2015).
31. Battaglia, G. & Joos, F. Hazards of decreasing marine oxygen: the near-term and millennial-scale benefits of meeting the Paris climate targets. *Earth Syst. Dynam.* **9**, 797–816 (2018).
32. Levin, L. A. Manifestation, drivers, and emergence of open ocean deoxygenation. *Annu. Rev. Mar. Sci.* **10**, 229–260 (2018).
33. Brennecka, G. A., Herrmann, A. D., Algeo, T. J. & Anbar, A. D. Rapid expansion of oceanic anoxia immediately before the end-Permian mass extinction. *Proc. Natl Acad. Sci. USA* **108**, 17631–17634 (2011).
34. Steffen, W. et al. Trajectories of the earth system in the anthropocene. *Proc. Natl Acad. Sci. USA* **115**, 8252–8259 (2018).
35. Holzer, M., Chamberlain, M. A. & Matear, R. J. Climate-driven changes in the ocean's ventilation pathways and time scales diagnosed from transport matrices. *J. Geophys. Res. Oceans* **125**, e2020JC016414 (2020).

https://doi.org/10.1038/s41558-022-01555-7

36. Plattner, G. K. et al. Long-term climate commitments projected with climate–carbon cycle models. *J. Clim.* **21**, 2721–2751 (2008).
37. Clark, P. U. et al. Consequences of twenty-first-century policy for multi-millennial climate and sea-level change. *Nat. Clim. Change* **6**, 360–369 (2016).
38. Frölicher, T. & Paynter, D. J. Extending the relationship between global warming and cumulative carbon emissions to multi-millennial timescales. *Environ. Res. Lett.* **10**, 075002 (2015).
39. Hajima, T. et al. Millennium timescale experiments on climate–carbon cycle with doubled $CO_2$ concentration. *Prog. Earth Planet. Sci.* **7**, 40 (2020).
40. Kwiatkowski, L. et al. Twenty-first century ocean warming, acidification, deoxygenation, and upper-ocean nutrient and primary production decline from CMIP6 model projections. *Biogeosciences* **17**, 3439–3470 (2020).
41. Hu, A., Meehl, G. A., Han, W. & Yin, J. Transient response of the MOC and climate to potential melting of the Greenland Ice Sheet in the 21st century. *Geophys. Res. Lett.* **36**, L10707 (2009).
42. Lago, V. & England, M. H. Projected slowdown of Antarctic bottom water formation in response to amplified meltwater contributions. *J. Clim.* **32**, 6319–6335 (2019).
43. Kwiatkowski, L. et al. Decline in Atlantic primary production accelerated by Greenland Ice Sheet melt. *Geophys. Res. Lett.* **46**, 11347–11357 (2019).
44. Mackie, S., Smith, I. J., Ridley, J. K., Stevens, D. P. & Langhorne, P. J. Climate response to increasing Antarctic iceberg and ice shelf melt. *J. Clim.* **33**, 8917–8938 (2020).

**Publisher's note** Springer Nature remains neutral with regard to jurisdictional claims in published maps and institutional affiliations.

Springer Nature or its licensor (e.g. a society or other partner) holds exclusive rights to this article under a publishing agreement with the author(s) or other rightsholder(s); author self-archiving of the accepted manuscript version of this article is solely governed by the terms of such publishing agreement and applicable law.

© The Author(s), under exclusive licence to Springer Nature Limited 2022

# Methods

## The CMIP5 and CMIP6 ensembles

We analyse simulations from a set of 24 ESMs that were submitted to the Earth System Grid Federation as a part of CMIP5 and 36 ESMs that participated in CMIP6 to study the changing of overturning circulation and carbon sequestration under the business-as-usual scenarios in CMIP5 (RCP8.5–ECP8.5) and three warming scenarios from CMIP6 (SSP5–8.5 + long-term extensions, SSP2–4.5, SSP1–2.6) (Supplementary Tables 1 and 2). We use the MOC output variable 'msftmz' and 'msftyz' if available and integrate the meridional transport output 'vmo' for the models not having 'msftmz' or 'msftyz'. Required physical ocean variables also included potential temperature and salinity to compute the density for assessing the ocean stratification. SMOC rate is defined as the maximum cell strength at 30° S over depths of 2,500–5,000 m. AMOC rate is defined as the maximum overturning between 0–3,000 m at 30° N. The relative contributions of AMOC and SMOC are dependent on the boundary between the upper and abyssal cells of MOC, defined as the depth at the Equator where the stream function is equal to zero. The AABW export from the Southern Ocean is defined as the net northward bottom flow across 50° S in each model.

We also use CMIP6 models to study the carbon sequestration by dividing the dissolved inorganic carbon (variable 'dissic') into regenerated and pre-formed fractions based on the AOU:

$$\mathrm{regDIC} = r_{\mathrm{C:O_2}} \times \mathrm{AOU}$$

$$\mathrm{preDIC} = \mathrm{DIC} - \mathrm{regDIC}$$

where AOU = $O_2$sat − $O_2$, and $O_2$sat is the saturation dissolved oxygen concentration of a water parcel in contact with the atmosphere. The oxygen variables in CMIP6 models are 'o2', and we computed the saturated $O_2$ ($O_2$sat) using the potential temperature and salinity to represent the effect of oxygen solubility changes. The regenerated dissolved inorganic phosphorus and nitrogen (DIP and DIN) are thus defined as:

$$\mathrm{regDIP} = r_{\mathrm{P:C}} \times \mathrm{regDIC}$$

$$\mathrm{regDIN} = r_{\mathrm{N:C}} \times \mathrm{regDIC}$$

where $r_{\mathrm{P:C}} = 1/117$, $r_{\mathrm{N:C}} = 16/117$and $r_{\mathrm{C:O2}} = 117/138$are fixed stoichiometric ratios[45]. The pre-formed fraction of DIP and DIN are thus defined as:

$$\mathrm{preDIP} = \mathrm{DIP} - \mathrm{regDIP}$$

$$\mathrm{preDIN} = \mathrm{DIN} - \mathrm{regDIN}$$

where DIP and DIN are retrieved from CESMv1-RCP8.5 outputs directly. For the models with the remineralization variable 'bddtdic' (MPI-ESM1-2-HR, MPI-ESM1-2-LR and IPSL-CM6A-LR), we separate the change in the deep-ocean regenerated DIC sequestration into contributions from biological and physical processes. Relevant output from the CMIP5 and CMIP6 models are available from the ESGF (https://www.earthsystemgrid.org).

## CMIP5 Community Earth System Model (CESMv1) RCP8.5–ECP8.5 Simulation

The CESMv1-RCP8.5 was used for CMIP5 and it simulates multiple plankton functional groups, key growth-limiting nutrients (nitrogen, phosphorus, iron, silicon), carbon, alkalinity, and oxygen[45]. The circulation is simulated using CCSM4 ocean component[46,47]. The model configuration details and spin up were previously reported[48] along with analysis of the historical uptake and storage of anthropogenic $CO_2$ in the oceans[49]. Evaluation of the marine ecosystem dynamics, biogeochemistry, and climate change impacts under RCP4.5 and RCP8.5 up to the year 2100 have been documented[50,51], and were extended to 2300 along the RCP8.5–ECP8.5 scenario[12,52]. We build on these previous analyses of this simulation, and compare with the CMIP6 results. RCP8.5–ECP8.5 is a high-end, emissions-as-usual scenario with prescribed atmospheric $CO_2$ values reaching 1962 ppm before levelling off for the last 50 years of the simulation. It was part of the CMIP5 simulations. Additional CESM documentation and source code are available online (www2.cesm.ucar.edu), and the model output files from this simulation are available through the ESGF data delivery system at (https://www.earthsystemgrid.org/dataset/ucar.cgd.ccsm4.randerson2015.html).

In the RCP8.5–ECP8.5 simulation, global mean surface air temperature increases 9.6 °C, warming more than 25 °C in polar regions[52]. We previously documented large increases in net primary production and export production in the high-latitude Southern Ocean driven by climate forcings (warming surface waters, declining sea ice cover, shifting winds), which stripped out a higher percentage of the nutrients upwelling at the Antarctic Divergence, reducing the northward flow of nutrients in the surface Ekman layer. The increased export production sinking into the upwelling waters drives a subsurface nutrient build-up (~100–1,000 m, 'nutrient trapping')[12]. Subsurface concentrations of nitrate, phosphate and silicate in this trapping region increase substantially and are still rising at the end of the simulation in the year 2300. Upper-ocean nutrient concentrations declined everywhere outside the Southern Ocean, leading to steady declines in biological production and export to the ocean interior. By 2300, global-scale net primary production decreases by 15%, and the global carbon export at 100 m declines by 30% (ref. 12).

## Development of the offline tracer transport model

It is difficult to separate the roles of the changing physical circulation from the changing biological processes using standard climate model output. We, therefore, constructed an offline tracer transport model from which we diagnose the separate effects of the changes in the circulation and the changes of the biogeochemical transformations. To this end, we retrieved the velocity field and diffusivity coefficients from the CESMv1-RCP8.5 output and constructed a time-dependent tracer transport operator

$$\boldsymbol{T}(t) \equiv \nabla \cdot [\boldsymbol{u}(t) - \boldsymbol{K}(t) \cdot \nabla]$$

with a one-year time resolution, that is, $\boldsymbol{T}(t)$consists of a series of sparse matrices, one per year, in which annual averages replace the continuous $\boldsymbol{u}(t)$ and $\boldsymbol{K}(t)$. No-flux conditions are built into the operator at all the solid basin boundaries and the sea surface. The parent ocean model in CESMv1 is POP2 (ref. 47).

On the discretized model mesh, tracer fields are represented by a column vector whose components represent the tracer concentrations at the mesh points. Multiplication of such a vector by $\boldsymbol{T}(t)$ yields the advective–diffusive flux divergence of the tracer. For example, if $c(t)$ represents a tracer concentration field with source minus sink given by $S(t)$, then the time evolution of $c$ is governed by the following system of ordinary differential equations

$$\frac{\mathrm{d}c}{\mathrm{d}t} + \boldsymbol{T}(t)\,c = S(t). \tag{1}$$

To separate the contribution of changing circulation from changing export production on the carbon storage in the deep ocean, we perform offline simulations using modified versions of equation (1) as described below.

## Partitioning regenerated and pre-formed DIC in CESMv1-RCP8.5 with the offline model

When studying the impacts of overturning circulation and climate change on ocean tracers, it is often helpful to partition the tracers into their regenerated and pre-formed components. Regenerated

https://doi.org/10.1038/s41558-022-01555-7

DIC consists of inorganic carbon that was remineralized from organic carbon or $CaCO_3$ in the ocean interior. When DIC comes into contact with the surface layer where it can participate in the air–sea exchange of $CO_2$, it is relabelled as pre-formed DIC. The contribution of dissolved organic carbon to the deep export is small, and it is neglected in this study. We achieve this relabelling using a short restoring timescale of one day. Thus, the governing equation for regenerated DIC is given by

$$\frac{\partial c_{\mathrm{reg}}}{\partial t} = -\boldsymbol{T}(t)\, c_{\mathrm{reg}} - \boldsymbol{L} c_{\mathrm{reg}} + S(t), \tag{2}$$

$$c_{\mathrm{reg}}(1850) = c_{\mathrm{reg},0}, \tag{3}$$

where $\boldsymbol{L}$ is a diagonal matrix operator with non-zero elements for diagonal entries corresponding to surface grid boxes. For those entries, the elements are given by the reciprocal of the surface restoring timescale. The source of regenerated carbon is given by

$$S(t) = r_{\mathrm{C:O_2}} \times \mathrm{OUR}(t) + D_{\mathrm{CaCO_3}}(t), \tag{4}$$

where the oxygen utilization rate, OUR $(t)$, and the calcium carbonate dissolution rate, $D_{\mathrm{CaCO_3}}(t)$, consist of annually averaged values extracted from the CESMv1-RCP8.5 model output.

The initial condition, specified in 1850, is obtained by assuming that the system was in a steady-state equilibrium for $t < 1850$ and then solving the resulting linear system

$$[\boldsymbol{T}(1850) + \boldsymbol{L}]\, c_{\mathrm{reg},0} = S(1850). \tag{5}$$

The governing equation for the pre-formed DIC is given by

$$\frac{\partial c_{\mathrm{pre}}}{\partial t} = -\boldsymbol{T}(t)\, c_{\mathrm{pre}} - \boldsymbol{L}\left(c_{\mathrm{pre}} - \mathrm{DIC}(t)\right), \tag{6}$$

$$c_{\mathrm{pre}}(1850) = c_{\mathrm{pre},0}, \tag{7}$$

where DIC $(t)$ is the total dissolved inorganic carbon extracted from the CESMv1-RCP8.5 output. The fast surface restoring term ensures that $c_{\mathrm{pre}} = \mathrm{DIC}(t)$ in the top layer of the model. Below the surface, $c_{\mathrm{pre}}(t) < \mathrm{DIC}(t)$ because of the absence of the regenerated carbon source in the $c_{\mathrm{pre}}$ governing equation. The initial condition, again specified in 1850, is obtained by assuming a pre-1850 steady state and solving the resulting linear system

$$[\boldsymbol{T}(1850) + \boldsymbol{L}]\, c_{\mathrm{pre},0} = \boldsymbol{L}\, \mathrm{DIC}(1850) \tag{8}$$

Note that because the tracer transport equation is linear, the regenerated carbon can be further decomposed into three parts

$$c_{\mathrm{reg}}(t) = c_{\mathrm{reg},0} + \Delta c_{\mathrm{reg},1} + \Delta c_{\mathrm{reg},2}, \tag{9}$$

where

$$\frac{\partial \Delta c_{\mathrm{reg},1}}{\partial t} = -\boldsymbol{T}(t)\, \Delta c_{\mathrm{reg},1} - \boldsymbol{L} \Delta c_{\mathrm{reg},1} + S(1850), \tag{10}$$

$$\Delta c_{\mathrm{reg},1}(1850) = 0, \tag{11}$$

corresponds to the time evolution of the regenerated carbon that was remineralized before 1850, and

$$\frac{\partial \Delta c_{\mathrm{reg},2}}{\partial t} = -\boldsymbol{T}(t)\, \Delta c_{\mathrm{reg},2} - \boldsymbol{L} \Delta c_{\mathrm{reg},2} + (S(t) - S(1850)), \tag{12}$$

$$\approx -\boldsymbol{T}(1850)\, \Delta c_{\mathrm{reg},2} - \boldsymbol{L} \Delta c_{\mathrm{reg},2} + (S(t) - S(1850)), \tag{13}$$

$$\Delta c_{\mathrm{reg},2}(1850) = 0, \tag{14}$$

corresponds to the time evolution of the carbon anomaly due to the change in the carbon regeneration rate after 1850. As shown by direct computation (Supplementary Information Fig. 1), the approximation in going from equation (12) to equation (13), where we replace the time-dependent transport operator with its 1850 value is a very good one. The negligible effect of the interaction between the time dependence of the transport operator and the time dependence of the biological source allows us to interpret $\Delta c_{\mathrm{reg},1}(t)$ and $\Delta c_{\mathrm{reg},2}(t)$ as a separation of the change in the regenerated carbon inventory into contributions due to the change in the physical circulation and the change in the biological production.

### Potential bias of the offline model and the traditional AOU method

We first compare CESMv1-RCP8.5 regenerated DIC accumulation computed from the offline model (equations (2) and (3)) and with the inorganic carbon regeneration computed using the AOU method (Supplementary Fig. 1). The patterns are very similar but, approximately 10–20% more regenerated DIC is sequestered in the deep ocean in the offline model estimate. The main reason for this difference is due to the neglect of carbon regeneration associated with the dissolution of $CaCO_3$ in the AOU calculation.

There are multiple possible errors in the offline model compared with the parent Parallel Ocean Program version 2 (POP2) ocean model. Before doing the offline tracer calculations, we coarse grained the tracer transport operator using the method from the POP2 nominal $1° \times 1°$ horizontal resolution to a roughly $2° \times 2°$ horizontal resolution[47]. We also coarse grained the time variable from a 3 hour time-step size in POP2 to a an annual time-step size for the offline model. Furthermore, the parent POP2 model in the CESMv1-RCP8.5 simulation has not reached complete equilibrium in 1850 causing a slight drift in the deep ocean that is not associated with imposed greenhouse forcing. In contrast, our offline calculations are based on an exact pre-industrial ($t < 1850$) steady state.

The traditional AOU method has been widely used to calculate the regenerated fraction of DIC in the ocean by assuming that surface oxygen concentration is saturated, which introduces some error to the estimation. We explicitly simulate pre-formed $O_2$ to compute the true oxygen utilization in the offline model to evaluate the uncertainties caused by the AOU method[53–60]. The accumulation rate of regenerated DIC computed from the AOU method compares well with the true oxygen utilization method in the whole water column (~5% uncertainties), even though the AOU methods underestimated the deep-ocean regenerated DIC by 0.03 Pg C–0.13 Pg C and overestimated the intermediate ocean regenerated DIC by 0.01 Pg C–0.12 Pg C depending on the century (Supplementary Fig. 2).

## Data availability

Relevant outputs from the CMIP5 and CMIP6 models are freely available from the Earth System Grid Federation (https://www.earthsystemgrid.org). The CESMv1 model outputs are available through the ESGF data delivery system at https://www.earthsystemgrid.org/dataset/ucar.cgd.ccsm4.randerson2015.html. The offline model outputs are available from Zenodo (https://doi.org/10.5281/zenodo.7402493). Source data are provided with this paper.

## Code availability

Codes used in the analysis of the CMIP datasets are available from Zenodo (https://doi.org/10.5281/zenodo.7402493).

## References


45. Moore, J. K., Doney, S. C. & Lindsay, K. Upper ocean ecosystem dynamics and iron cycling in a global three-dimensional model. *Glob. Biogeochem. Cycles* **18** (2004).
46. Danabasoglu, G. et al. The CCSM4 ocean component. *J. Clim.* **25**, 1361–1389 (2012).
47. Gent, P. R. et al. The community climate system model version 4. *J. Clim.* **24**, 4973–4991 (2011).
48. Lindsay, K. et al. Preindustrial-control and twentieth-century carbon cycle experiments with the Earth system model CESM1(BGC). *J. Clim.* **27**, 8981–9005 (2014).
49. Long, M. C., Lindsay, K., Peacock, S., Moore, J. K. & Doney, S. C. Twentieth-century oceanic carbon uptake and storage in CESM1(BGC). *J. Clim.* **26**, 6775–6800 (2013).
50. Moore, J. K., Lindsay, K., Doney, S. C., Long, M. C. & Misumi, K. Marine ecosystem dynamics and biogeochemical cycling in the Community Earth System Model [CESM1(BGC)]: comparison of the 1990s with the 2090s under the RCP4.5 and RCP8.5 scenarios. *J. Clim.* **26**, 9291–9312 (2013).
51. Misumi, K. et al. The iron budget in ocean surface waters in the 20$^{th}$ and 21$^{st}$ centuries: projections by the Community Earth System Model version 1. *Biogeosciences* **11**, 33–55 (2014).
52. Randerson, J. T. et al. Multicentury changes in ocean and land contributions to the climate–carbon feedback. *Glob. Biogeochem. Cycles* **29**, 744–759 (2015).
53. Ito, T., Follows, M. J. & Boyle, E. A. Is AOU a good measure of respiration in the oceans? *Geophys. Res. Lett.* **31**, 17 (2004).
54. Lumpkin, R. & Speer, K. Global ocean meridional overturning. *J. Phys. Oceanogr.* **37**, 2550–2562 (2007).
55. Talley, L. D. Closure of the global overturning circulation through the Indian, Pacific, and Southern Oceans: schematics and transports. *Oceanography* **26**, 80–97 (2013).
56. Meinen, C. S. et al. Meridional overturning circulation transport variability at 34.5° S during 2009–2017: baroclinic and barotropic flows and the dueling influence of the boundaries. *Geophys. Res. Lett.* **45**, 4180–4188 (2018).
57. McCarthy, G. D. et al. Measuring the Atlantic Meridional Overturning Circulation at 26° N. *Prog. Oceanogr.* **130**, 91–111 (2015).
58. Kunze, E. Internal-wave-driven mixing: global geography and budgets. *J. Phys. Oceanogr.* **47**, 1325–1345 (2017).
59. De Lavergne, C. et al. The impact of a variable mixing efficiency on the abyssal overturning. *J. Phys. Oceanogr.* **46**, 663–681 (2016).
60. Liu, Yi., Moore, J. K., Primeau, F., & Wang, W.-L. Reduced CO2 uptake and growing nutrient sequestration from slowing overturning circulation. *Zenodo* https://doi.org/10.5281/zenodo.7402493 (2022).


## Acknowledgements


We thank the thousands of scientists worldwide who contributed to the development of the Earth system models for CMIP and to carrying out the CMIP6 simulations. We received support from the Reducing Uncertainties in Biogeochemical Interactions through Synthesis and Computation Scientific Focus Area (RUBISCO SFA) under the Regional and Global Analysis Program Area (RGMA) and the Earth System Model Development Program Area (ESMD) in the Earth and Environmental Sciences Division of the Biological and Environmental Research Division of the US Department of Energy Office of Science. The Coupled Model Intercomparison Project received support from the World Climate Research Programme and the US Department of Energy's Program for Climate Model Diagnosis and Intercomparison. We acknowledge funding from US Department of Energy BER RGMA (RUBISCO SFA) (J.K.M., Y.L.), US Department of Energy DOE-BER ESMD grant DE-SC0016539 (J.K.M., F.P., W.L.W.), US Department of Energy DOE-BER ESMD grant DE-SC0021267 (F.P., J.K.M.) and US Department of Energy DOE-BER ESMD grant DE-SC0022177 (J.K.M., F.P.).


## Author contributions

Conceptualization: J.K.M., Y.L. and F.P. Data curation: Y.L. Formal analysis: Y.L., J.K.M., F.P. and W.L.W. Funding acquisition: J.K.M. and F.P. Investigation: Y.L., J.K.M., F.P. and W.L.W. Methodology: Y.L., J.K.M., F.P. and WLW. Project administration: J.K.M. Software: Y.L., F.P. and W.L.W. Writing–original draft: Y.L. and J.K.M. Writing–review and editing: J.K.M., Y.L., F.P. and W.L.W.

## Competing interests

The authors declare no competing interests.

## Additional information

**Extended data** is available for this paper at https://doi.org/10.1038/s41558-022-01555-7.

**Supplementary information** The online version contains supplementary material available at https://doi.org/10.1038/s41558-022-01555-7.

**Correspondence and requests for materials** should be addressed to Y. Liu or J. K. Moore.

**Peer review information** *Nature Climate Change* thanks the anonymous reviewers for their contribution to the peer review of this work.

**Reprints and permissions information** is available at www.nature.com/reprints.

 https://doi.org/10.1038/s41558-022-01555-7

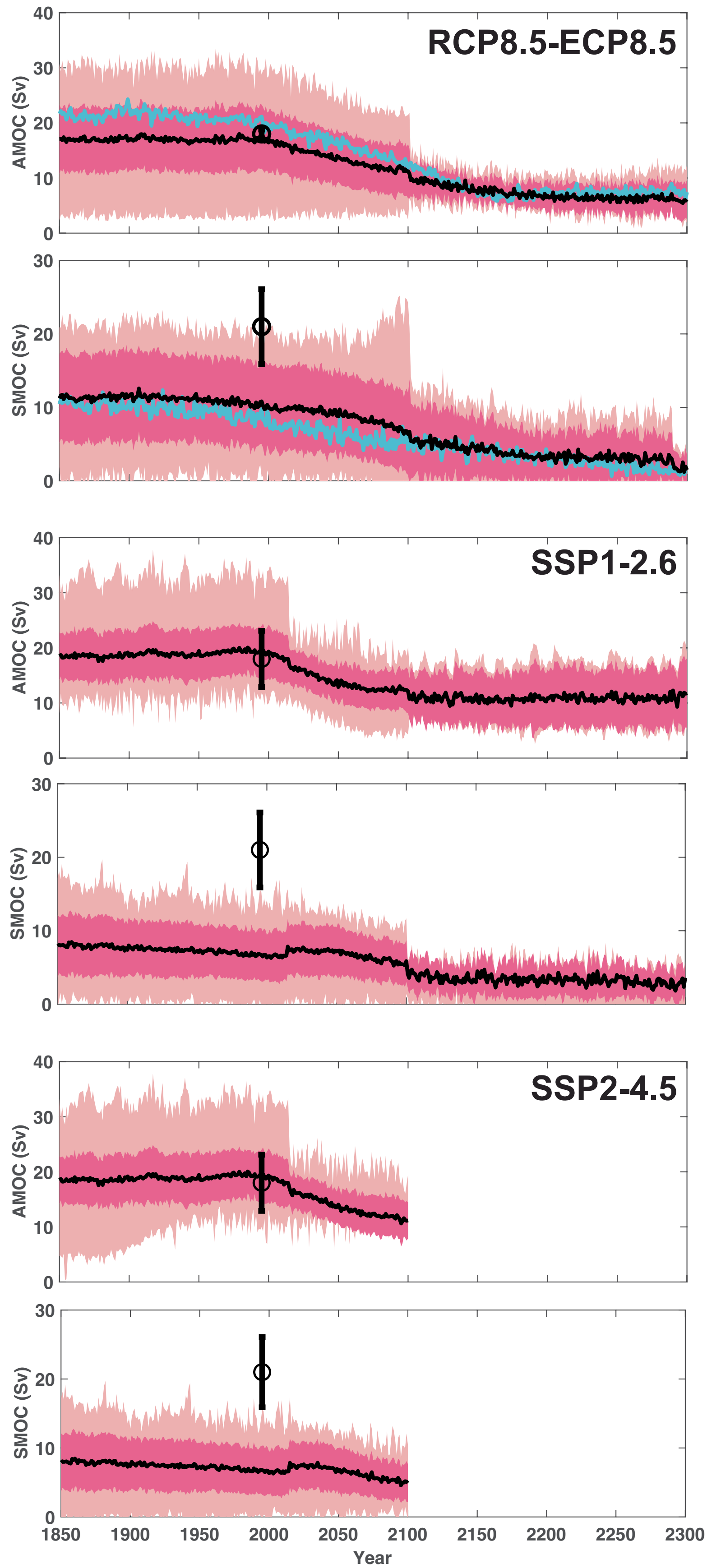


**Extended Data Fig. 1 | See next page for caption.**

https://doi.org/10.1038/s41558-022-01555-7

**Extended Data Fig. 1 | Slowdown of Meridional Overturning Circulation (MOC) in CMIP5 (RCP8.5-ECP8.5) and CMIP6 (SSP1-2.6 and SSP2-4.5).** The Atlantic Meridional Overturning Circulation (AMOC) and the Southern Meridional Overturning Circulation (SMOC) calculated from available CMIP5 models and CMIP6 models (Sv) are shown. The CESMv1 simulation is included and shown here as light blue line. Black lines show the multi-model mean, and light and dark pink shading indicate the range and one standard deviation of the overturning circulation. Black circles and error bars show mean and standard deviation of the observational estimates of MOC rates in Supplementary Table 1.

https://doi.org/10.1038/s41558-022-01555-7

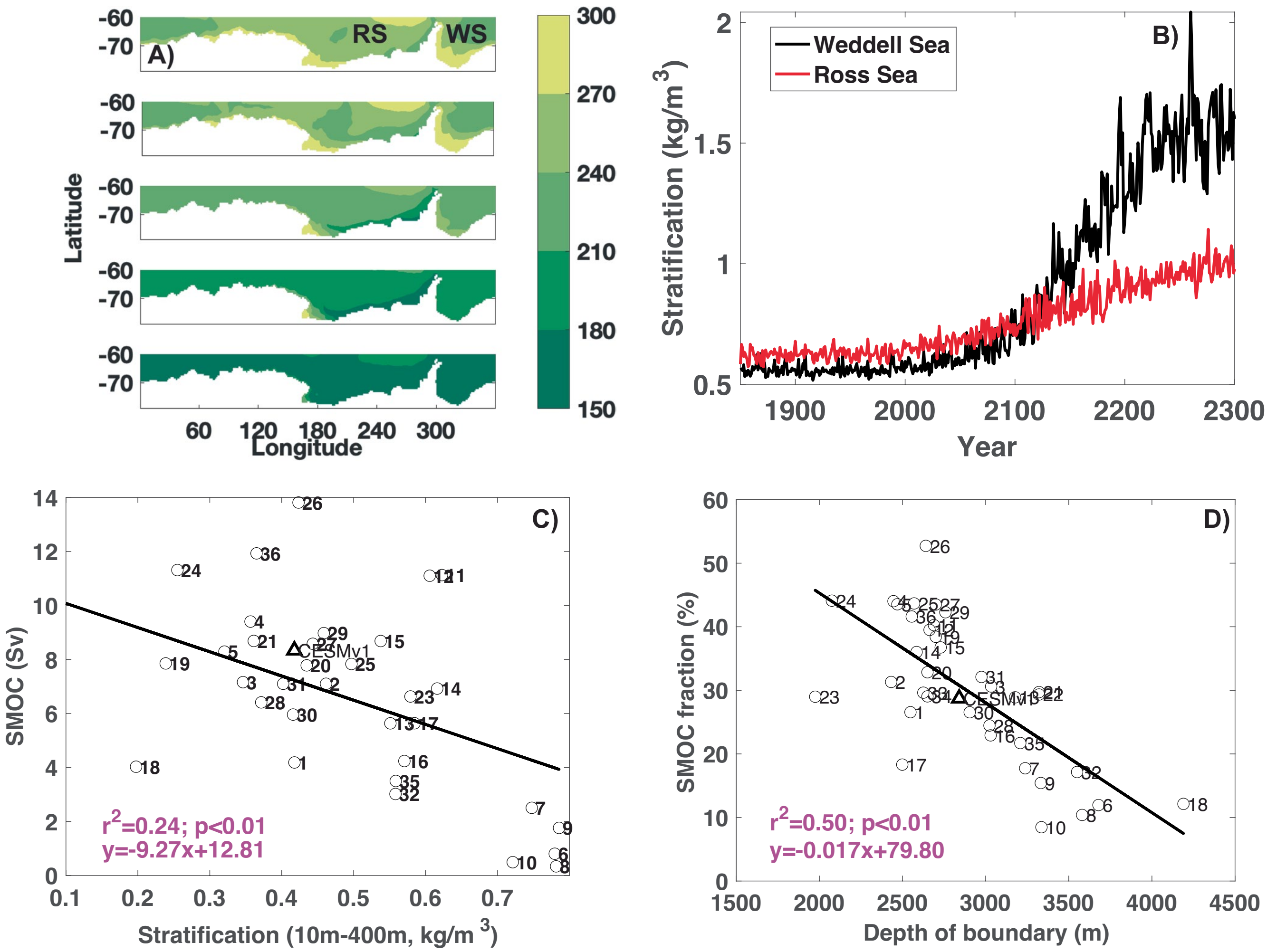


**Extended Data Fig. 2 | Declining Southern Ocean AABW Formation and SMOC.** Dissolved oxygen distributions (mmol/m$^3$) at shelf depths (200–400 m) are shown in panel A for decades (1850s, 1990s, 2090 s, 2190 s, and 2290 s) with time series of mean stratification (kg/m$^3$, calculated by $\rho_{400m} - \rho_{0m}$) in the Weddell Sea (black line) and Ross Sea (red line, B). Panel C and D compare mean stratification (south of 60 °S) versus the SMOC rates (Sv), and mean depth boundary between the AMOC and the SMOC compared with the SMOC fraction of total global overturning circulation in the 1990s for the CMIP6 models. The number in C) and D) indicate the number of models in Supplementary Table 1. The 'RS' and 'WS' represent Ross Sea and Weddell Sea.

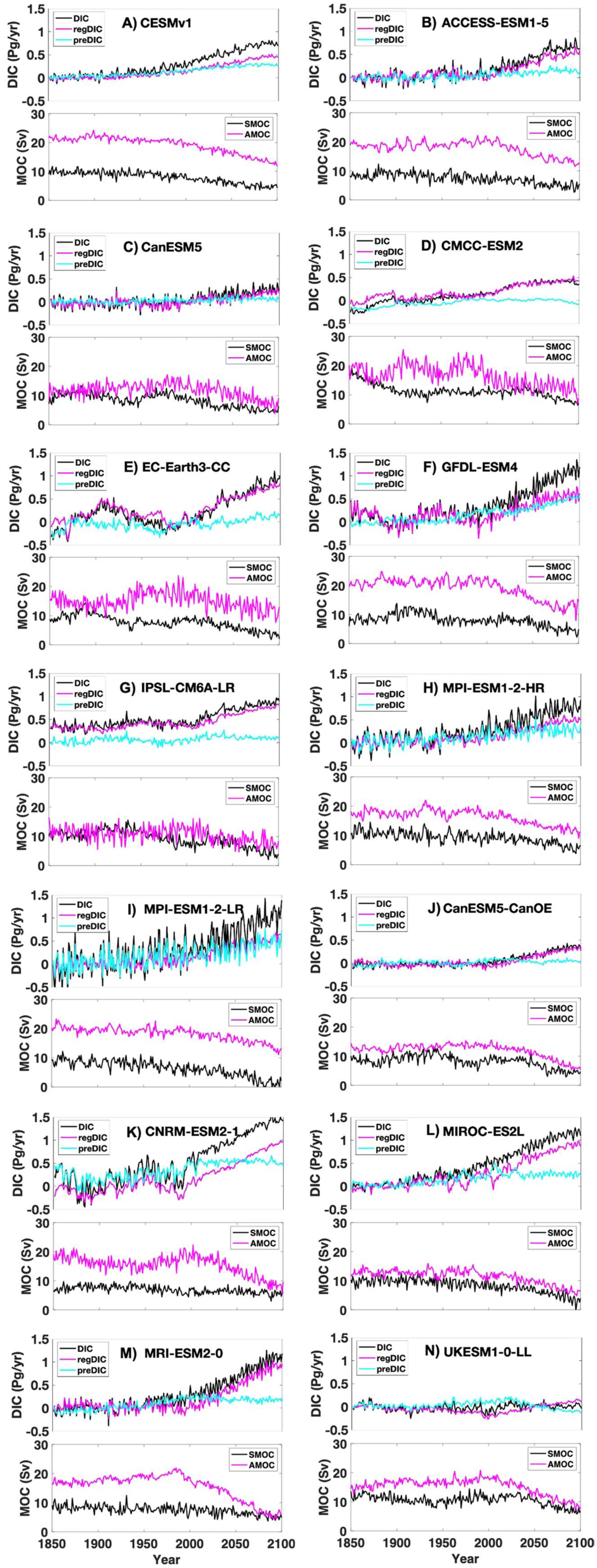


**Extended Data Fig. 3 | See next page for caption.**

https://doi.org/10.1038/s41558-022-01555-7

**Extended Data Fig. 3 | Deep ocean carbon accumulation (> 2000m) in CESMv1 RCP8.5 and 13 CMIP6 models under the SSP5-8.5 warming scenario.** The time series of DIC partitioning in CESMv1 (A), ACCESS-ESM1-5 (B), CanESM5 (C), CMCC-ESM2 (D), EC-Earth3-CC (E), GFDL-ESM4 (F), IPSL-CM6A-LR (G), MPI-ESM1-2-HR (H), MPI-ESM1-2-LR (I), CanESM5-CanOE (J), CNRM-ESM2-1 (K), MIROC-ES2L (L), MRI-ESM2-0 (M) and UKESM1-0-LL (N), where the black, red and blue line represents the total DIC, regenerated DIC and preformed DIC accumulation below 2000m depth (PgC/yr). Changing rates of the Southern-sourced Meridional Overturning Circulation (SMOC) and the Atlantic Meridional Overturning Circulation (AMOC) are also shown for each model.

https://doi.org/10.1038/s41558-022-01555-7

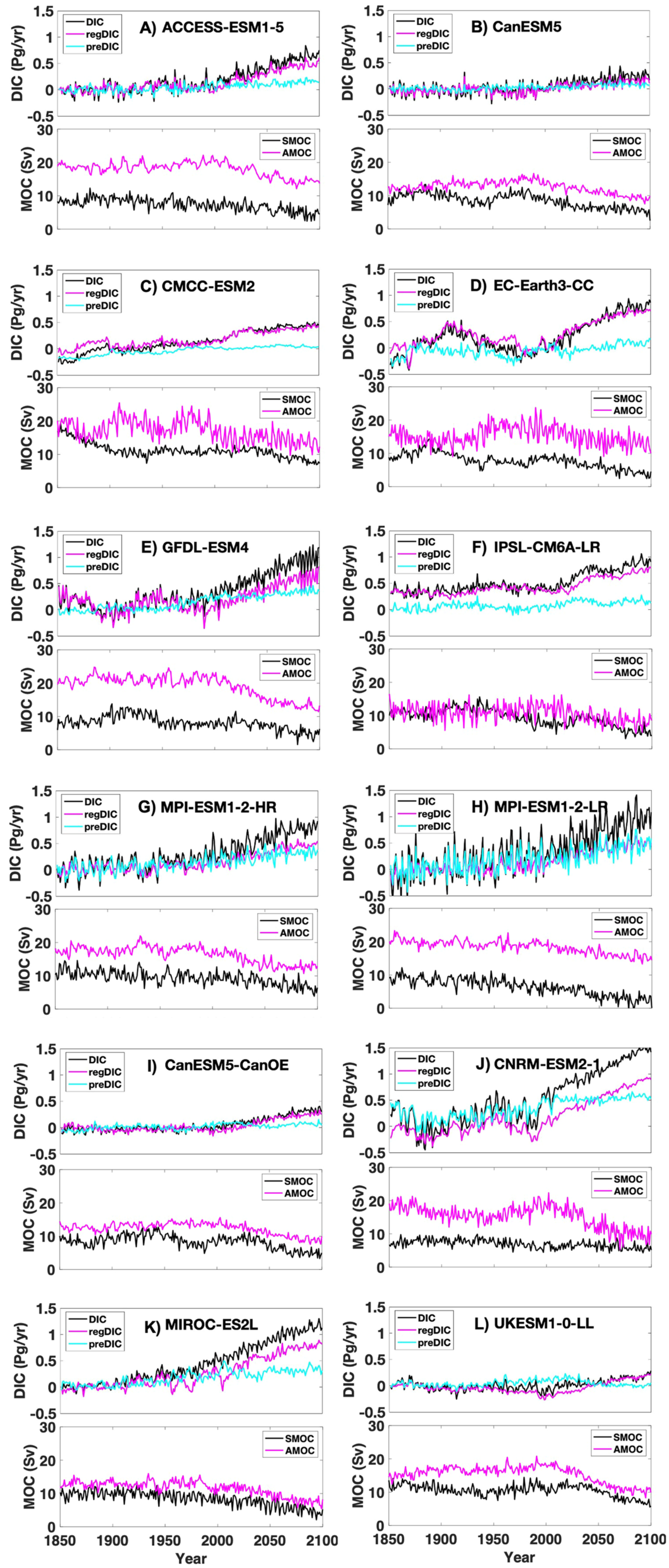


**Extended Data Fig. 4 | See next page for caption.**

https://doi.org/10.1038/s41558-022-01555-7

**Extended Data Fig. 4 | Deep ocean carbon accumulation and meridional overturning rates in twelve CMIP6 models under SSP2-4.5 scenario.** The time series of DIC partitioning in ACCESS-ESM1-5 (A), CanESM5 (B), CMCC-ESM2 (C), EC-Earth3-CC (D), GFDL-ESM4 (E), IPSL-CM6A-LR (F), MPI-ESM1-2-HR (G), MPI-ESM1-2-LR (H), CanESM5-CanOE (I), CNRM-ESM2-1 (J), MIROC-ES2L (K) and UKESM1-0-LL(L), where the black, red and blue line represents the total DIC, regenerated DIC and preformed DIC accumulation below 2000m depth (PgC/yr). Changing rates of the Southern-sourced Meridional Overturning Circulation (SMOC) and the Atlantic Meridional Overturning Circulation (AMOC) are also shown for each model.

https://doi.org/10.1038/s41558-022-01555-7

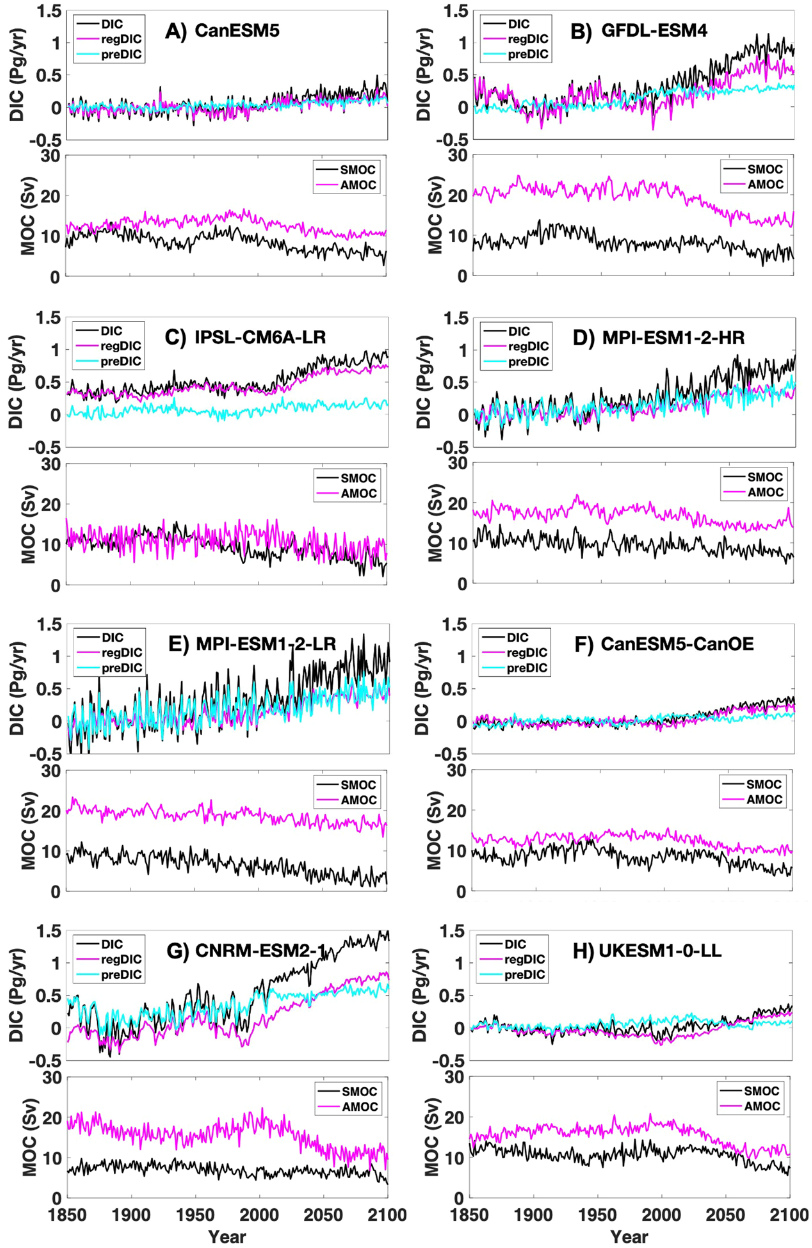


**Extended Data Fig. 5 | Deep ocean carbon accumulation and meridional overturning rates in eight CMIP6 models under the SSP1-2.6 warming scenario.** The time series of DIC partitioning in CanESM5 (A), GFDL-ESM4 (B), IPSL-CM6A-LR (C), MPI-ESM1-2-HR (D), MPI-ESM1-2-LR (E), CanESM5-CanOE (F), CNRM-ESM2-1 (G) and UKESM1-0-LL (H), where the black, red and blue lines represent the total DIC, regenerated DIC and preformed DIC below 2000m depth (PgC/yr). Changing rates of the Southern-sourced Meridional Overturning Circulation (SMOC) and the Atlantic Meridional Overturning Circulation (AMOC) are also shown for each model.

https://doi.org/10.1038/s41558-022-01555-7

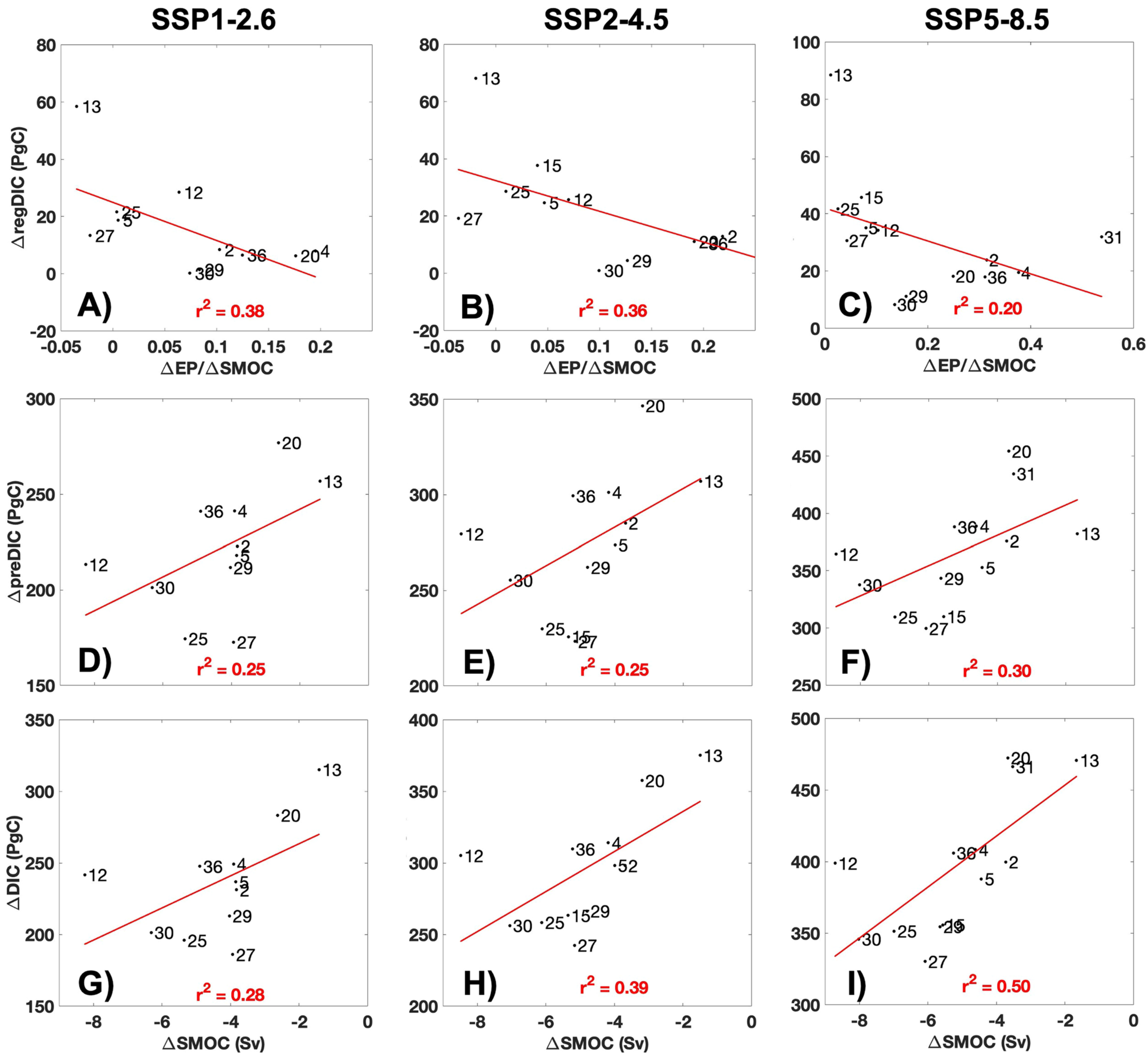


**Extended Data Fig. 6 | Slowing SMOC rates on intermediate ocean carbon uptake.** The intermediate water (100–2000 m) storage of regenerated dissolved inorganic carbon (DIC) (top row, A-C), preformed DIC (middle row, D-F), and total DIC (bottom row, G-I) by year 2100 (2080–2099 compared to 1850–1869) from eleven CMIP6 SSP1-2.6 projections (left column), twelve CMIP6 SSP2-4.5 projections (middle column), and thirteen CMIP6 SSP5-8.5 projections (right column) are compared with the relative declines of export production and SMOC rates (regenerated DIC) and declines in SMOC rate (preformed DIC and total DIC) by year 2100 (2080-2099 compared to 1850–1869). Plotted numbers indicate model number in Supplementary Table 1.

https://doi.org/10.1038/s41558-022-01555-7

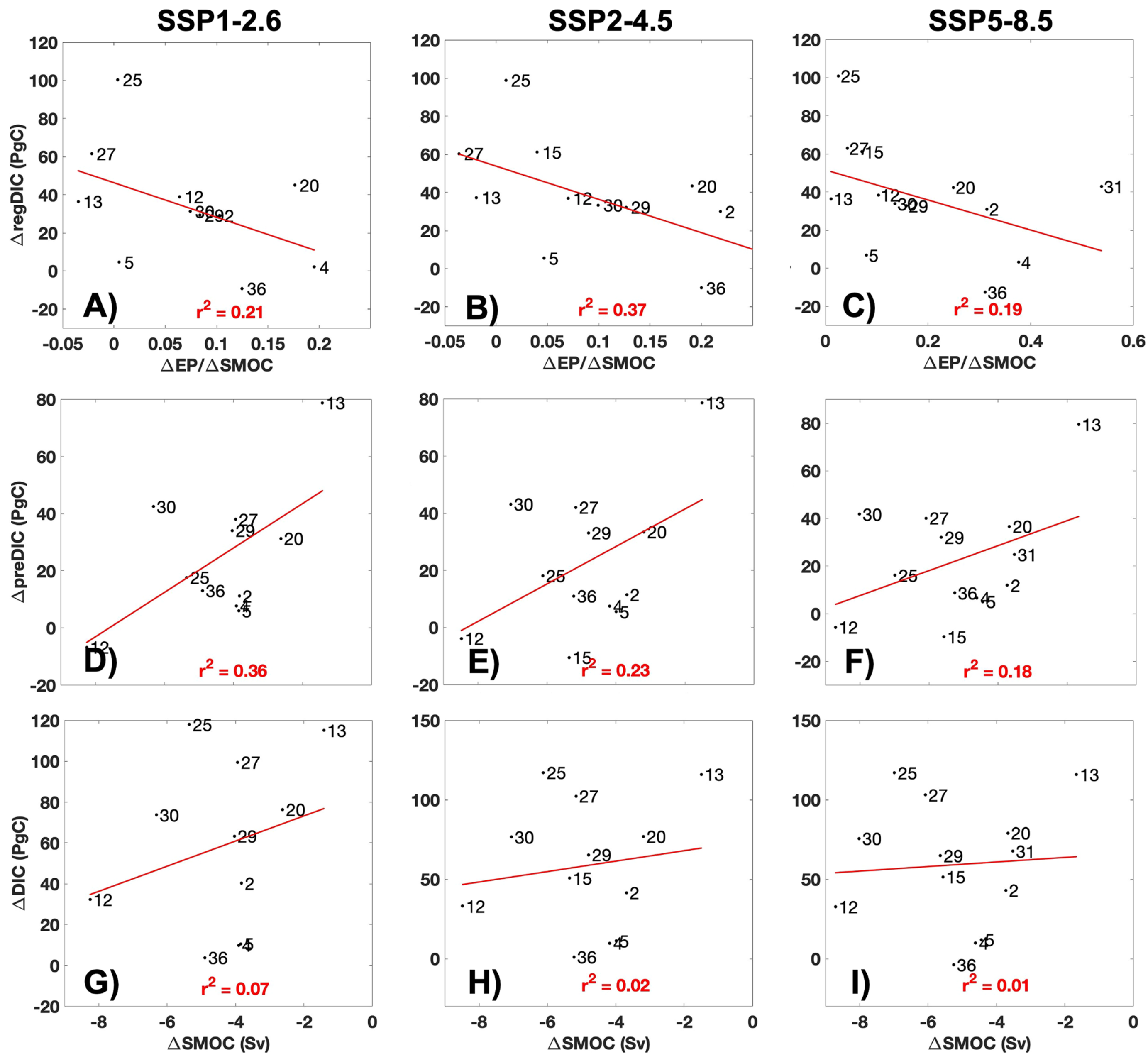


**Extended Data Fig. 7 | Slowing SMOC rates on deep ocean carbon uptake.** The deep water (>2000m) storage of regenerated dissolved inorganic carbon (DIC) (top row, A-C), preformed DIC (middle row, D-F), and total DIC (bottom row, G-I) by year 2100 (2080–2099 compared to 1850–1869) from eleven CMIP6 SSP1-2.6 projections (left column), twelve CMIP6 SSP2-4.5 projections (middle column), and thirteen CMIP6 SSP5-8.5 projections (right column) are compared with the relative declines of export production and SMOC rates (regenerated DIC) and declines in SMOC rate (preformed DIC and total DIC) by year 2100 (2080–2099 compared to 1850–1869). Plotted numbers indicate model number in Supplementary Table 1.

https://doi.org/10.1038/s41558-022-01555-7

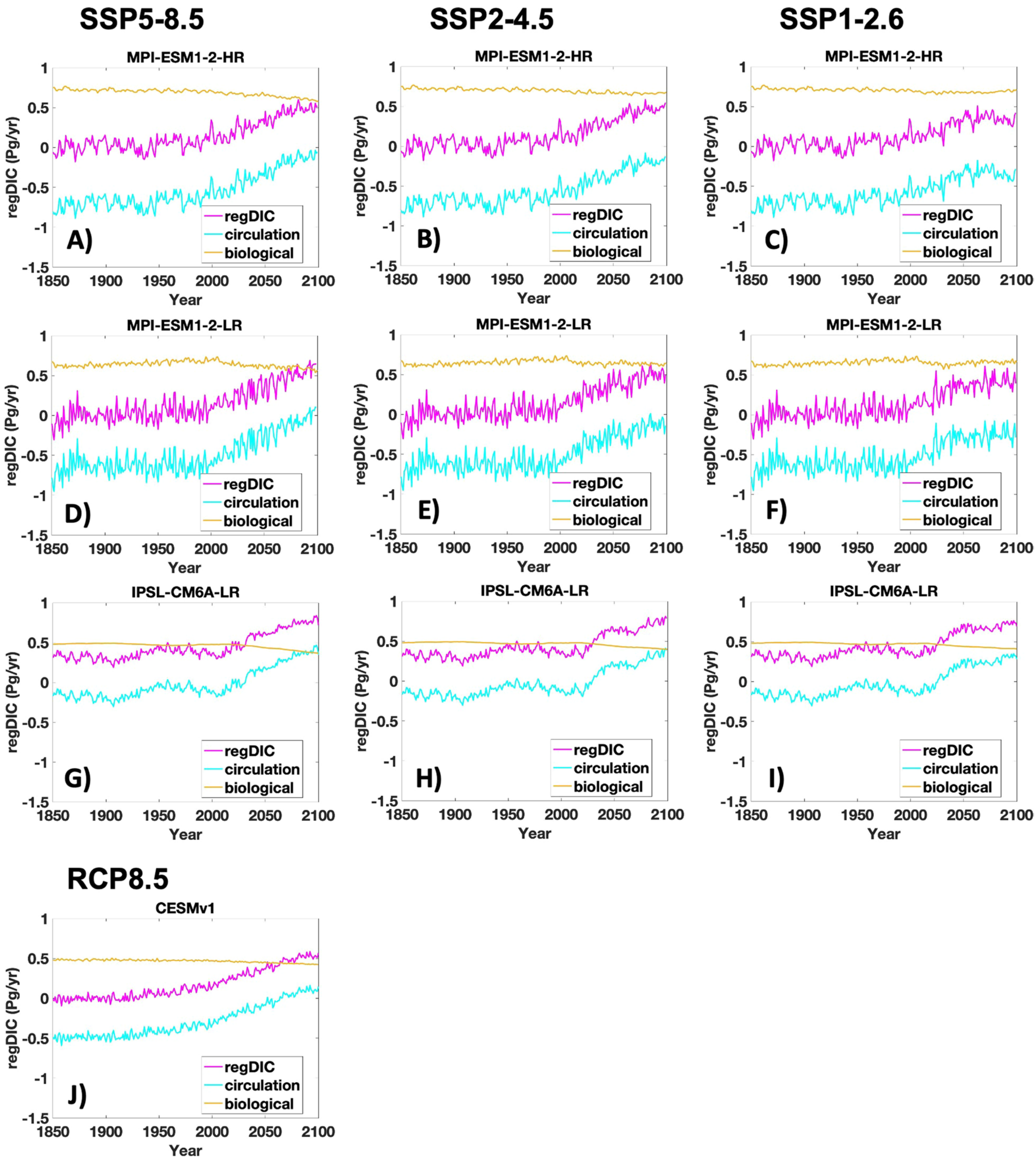


**Extended Data Fig. 8 | Separating biology and circulation impacts on regenerated DIC accumulation in the deep ocean.** The contribution of varying circulation and sinking biological export to the deep ocean (> 2000m) regenerated DIC accumulation for MPI-ESM1-2-HR (A, B, C), MPI-ESM1-2-LR (D, E, F) and IPSL-CM6A-LR (G, H, I) from the CMIP6 under SSP5-8.5 (A, D, G), SSP2-4.5 (B, E, H), SSP1-2.6 (C, F, I) climate scenarios. The CESMv1 results from the CMIP5 under RCP8.5 (J) are also shown.